PHYSICAL REVIEW B VOLUME 3, NUMBER 2 15 JANUARY 1971

Cyclotron Resonance and the Cohen Nonellipsoidal Nonparabolic Model for Bismuth. II. Limiting-Point Masses*

R. J. Dinger and A. W. Lawson
Department of Physics, University of California, Riverside, California 92502
(Received 13 April 1970)

An equation for the limiting-point (LP) cyclotron effective mass as a function of magnetic field direction is derived for the Cohen nonellipsoidal nonparabolic (NENP) model of the electron Fermi surface of Bi. The general NENP equation is used, in which the L-point valence and conduction bands are not assumed identical. For some orientations of the magnetic field, the NENP model, unlike the ellipsoidal nonparabolic (ENP) model, predicts a LP mass larger than the central-orbit extremal mass by as much as a factor of 2 for pure Bi. The previously published LP-mass data of Edel'man and Khaikin are found to be in good agreement qualitatively with the NENP model; the NENP fit is clearly superior to the ENP fit. Attempts to determine unambiguous values for the adjustable band parameters in the NENP model by fitting the experimental data were unsuccessful, but in general the experimental data indicate that the L-point valence and conduction bands have essentially identical parameters. For identical bands, the value $E_F/E_g = 0.50$ is required in order to fit the data.

I. INTRODUCTION

Edel'man and Khaikin[1] (EK) have published the most accurate and definitive study of cyclotron resonance in Bi to date. Their graphs showing the dependence of the cyclotron effective masses upon magnetic field direction contain numerous instances in which the data points deviate substantially from the curves derived from the ellipsoidal parabolic[2] (EP) or ellipsoidal nonparabolic[3] (ENP) models.[4] These are the models often used to interpret Fermi-surface data for Bi and dilute Bi alloys. In an earlier paper[5] (hereafter referred to as I), we interpreted EK's effective-mass data due to electrons whose orbits were extremal (central orbit, or CO, masses) on the basis of the Cohen nonellipsoidal nonparabolic (NENP) model.[6] We found that, in one of the two cases where deviations existed, the data points fit the NENP model very well, and that the value of E/E_g (E_g equals the energy gap between the L-point valence and conduction bands) required agreed well with the value derived from magneto-optical measurements.[7] In the other case the data points fit the NENP model no better or worse than the ENP model. These results, taken in conjunction with the cyclotron-resonance data of Kao[8] and the deHaas–van Alphen results of Bhargava,[9] both of which were also investigated in I, allowed us to conclude that the NENP model gives a better description of the Fermi surface in Bi than does the ENP model.

EK were also successful in observing cyclotron resonance due to electrons at the limiting points, i.e., those points where the Fermi velocity is parallel to the magnetic field. Their results are very intriguing, for at some orientations of the magnetic field the limiting-point (LP) mass is as much as 33% larger than the CO mass. It is easy to show that the ENP model predicts that the CO and LP masses are identical for *all* orientations of the magnetic field. The 33% difference is of course far outside any conceivable random experimental errors and hence the ENP model fails convincingly in accounting for the LP data.

The purpose of this paper is to compare the LP-mass data of EK with the NENP model. Our basic motivation is to verify with higher confidence the validity of the NENP model for Bi. In I, both the number of cases which could be analyzed and the deviations involved between the two models (at best, about 8%) were rather small. For EK's LP-mass data, however, both these objections are overcome: There are four cases presented by EK which can be analyzed, and the deviations involved are as much as 33%, as mentioned above. Additional motivation is supplied by a recent paper by Bate, Einspruch, and May (BEM)[10] in which doping of Bi with dilute concentrations of Sn was used to lower the Fermi energy into the L-point valence band. Their measurements on the holes thus produced at the top of the L-point valence band indicate that this band is far from being a "mirror" band of the L-point conduction band. This finding is in contradiction to many experiments[7,11–14] which indicate that the L-point valence and conduction bands have identical parameters. Fitting the LP-mass data of EK to the NENP model allows conclusions to be drawn about the L-point valence band, because in its most general form the NENP model does not require the valence and conduction bands to have identical parameters, as does the ENP model.

In Sec. II we derive an equation for the LP-mass

anisotropy and in Secs. III and IV compare the data of EK with this equation. As in I, we find that the experimental data are in better agreement with the NENP model than the ENP model, although there are some inconsistencies.

II. THEORY

The basic features of the Fermi surface of Bi are summarized in I, and here we simply repeat the equations necessary for what follows. The energy-momentum dispersion relation for the ENP model is given by

$$E\left(1+\frac{E}{E_g}\right)=\frac{p_1^2}{2m_1}+\frac{p_2^2}{2m_2}+\frac{p_3^2}{2m_3} \tag{1}$$

and for the NENP model by

$$\left(E-\frac{p_2^2}{2m_2}\right)\left(1+\frac{E}{E_g}-\frac{p_2^2}{2m_2'E_g}\right)=\frac{p_1^2}{2m_1}+\frac{p_3^2}{2m_3}. \tag{2}$$

E_g is the energy gap between the valence and conduction bands; m_1, m_2, and m_3 are the effective-mass tensor components at the bottom of the L-point conduction band; and m_2' is an effective-mass tensor component at the top of the L-point valence band. In I we began by setting $m_2=m_2'$; however, for reasons given in Sec. I, we will not assume that m_2 and m_2' are the same in this paper. For computational purposes we can put Eq. (2) in a more convenient form:

$$E(1+\lambda)-\gamma\frac{p_2^2}{2m_2}-r\frac{p_2^4}{4m_2^2E_g}=\frac{p_1^2}{2m_1}+\frac{p_3^2}{2m_3}, \tag{3}$$

where

$$r=m_2/m_2', \quad \lambda=E/E_g, \quad \gamma=1+\lambda-\lambda r.$$

Equations (1) and (3) are both written in the principal-axis system of any one of the three ellipsoids[15] which make up the electron Fermi surface of Bi. One must be careful when comparing experimental data with Eqs. (1) and (3), since the measured cyclotron effective masses are energy dependent and the derived values of m_1, m_2, m_2', and m_3 will depend on the value of E/E_g used. In the Appendix we derive equations for the relationship between the measured cyclotron effective masses and the effective-mass tensor components.

The importance of limiting points in cyclotron resonance is discussed in some detail by Azbel' and Kaner.[16] The limiting points on any Fermi surface are defined as those points at which the electron velocity is parallel to the external magnetic field $\vec{H}$; since the velocity is always perpendicular to the Fermi surface, the surface itself is then perpendicular to $\vec{H}$ at the limiting points. As discussed in Ref. 16, the effective masses measured when $\vec{H}$ is oriented parallel to the microwave electric field E_{mw} are effective masses associated with electron orbits at or near the limiting points. Actually at the limiting point itself, one ceases to speak of "orbits," since the Larmor radius is zero. The "normal" Azbel'Kaner cyclotron-resonance geometry has E_{mw} perpendicular to $\vec{H}$ and is sensitive to CO effective masses.

In general the CO masses will be different from the LP masses. In the case of the ENP model [and more generally for any energy surface of the form $f(E)=\vec{p}\cdot\alpha\cdot\vec{p}$, where $f(E)$ equals any function of energy and α equals the inverse effective-mass tensor], however, the CO and LP masses are identical, as mentioned earlier. This is a well-known result, but we show it explicitly for the case given in Fig. 1 for comparison with a similar calculation which we will do for the NENP model. The area of the cross-hatched section is easily found from Eq. (1) to be

$$a=2\pi(m_1m_3)^{1/2}[E(1+E/E_g)-(p_3)_0^2/2m_3]. \tag{4}$$

Then, since the cyclotron-effective mass for a given orbit perpendicular to $\vec{H}$ is given by

$$m^*=\frac{1}{2\pi}\frac{\partial a}{\partial E}, \tag{5}$$

we have

$$m^*=(m_1m_3)^{1/2}(1+2E/E_g), \tag{6}$$

independent of $(p_3)_0$. Hence, the effective mass is the same at $(p_3)_0=0$ (CO mass) and $(p_3)_0=(p_3)_{max}$ (LP mass). A similar result holds for any orientation of $\vec{H}$.

We will now do an equivalent calculation for the NENP model. For simplicity we will take $m_2'=m_2$ for this particular calculation, since none of the conclusions are affected by doing this. Setting $p_3=(p_3)_0$ in Eq. (2), an equation in the two variables p_1 and p_2 is obtained. The area enclosed by this curve is then the area required for Eq. (5). The computation of this area proceeds in the same manner as the area calculation in I, except that the constants are somewhat different. We can take a shortcut to the result desired here in the following manner. Defining $R=(p_3)_0/(p_3)_{max}$, we can write for the NENP model

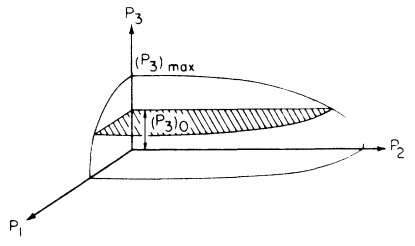

FIG. 1. Geometry for calculating the variation of the cyclotron effective mass as a function of $(p_3)_0$.

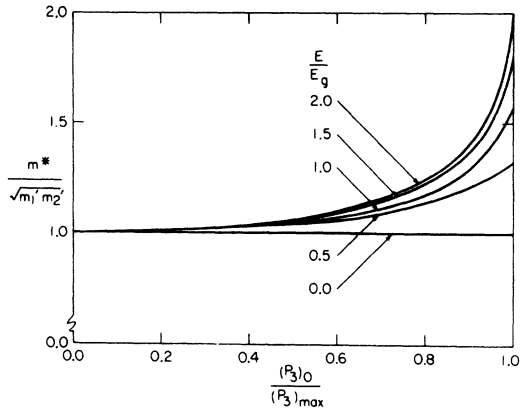

FIG. 2. Cyclotron effective mass vs $(p_3)_0$ in the NENP model, as given by Eq. (9) and Eqs. (A5) and (A6).

$$(p_3)_0^2 = 2m_3R^2E(1+E/E_g). \tag{7}$$

Substituting Eq. (7) into Eq. (2) with $p_3 = (p_3)_0$ and rearranging, we obtain

$$\frac{p_1^2}{2m_1}+\frac{p_2^2}{2m_2}=\frac{p_2^4}{4m_2^2E_g}+(1-R^2)E\left(1+\frac{E}{E_g}\right). \tag{8}$$

Equation (8) is identical to the equation of the curve enclosing the *extremal* area (i.e., the area with $p_3 = 0$) for this orientation of $\vec{H}$, except for the factor of $1-R^2$. Since this factor will in no way affect the energy derivative needed to compute the effective mass, the equation needed here can be obtained by (a) reducing the general equation for $m^*(\theta, \Omega)$ obtained in I [Eq. (7) in I] to the case where $\vec{H}$ is along axis 3 (i.e., set $\theta = \Omega = 0$) and then (b) replacing $(E/E_g)(1+E/E_g)$ by $(1-R^2) \times (E/E_g)(1+E/E_g)$. Doing (a) and (b), the following equation results:

$$m^*[(p_3)_0, E] = \frac{\sqrt{2}(1+2E/E_g)(m_1m_2)^{1/2}}{b^{1/4}}K[(1+\tau)^{-1/2}], \tag{9}$$

where

$$b = (1-R^2)(E/E_g)(1+E/E_g)+\tfrac{1}{4},$$

$$\tau = [(b)^{1/2}+\tfrac{1}{2}]/[(b)^{1/2}-\tfrac{1}{2}],$$

and K is the complete elliptic integral of the first kind.

Figure 2 is a plot of Eq. (9). The main conclusion to be drawn from these curves is that the LP mass is from 33 to 100% larger than the CO mass for E/E_g between 0.5 and 2.0. Since the ENP model corresponds to the case where the CO and LP masses are equal, there will be the same percentage differences between the ENP and NENP models. For the CO mass, on the other hand, the NENP and ENP masses differ by only about 8%. The observation of LP cyclotron resonance in pure Bi offers a sensitive method for testing the NENP model, and for establishing a value of the parameter E/E_g.

The above calculation is designed to show that one does expect an LP mass different from the CO mass in the NENP model. A full comparison with any experimental data requires an expression for $m^*_{\mathrm{LP}}(\alpha, \beta)$, where α and β are angles defining the direction of $\vec{H}$ with respect to the crystallographic axes [Fig. 3(a)]. Our approach here is the same as the approach used in I: We first compute $m^*_{\mathrm{LP}}(\theta, \Omega)$, where θ and Ω [Fig. 3(b)] are defined in the principal-axis system of any one of the three ellipsoids. The actual tilt and rotations about the trigonal axis of the ellipsoids are then accounted for by three transformations (one for each ellipsoid) from the principal-axis system to the crystallographic-axis system. We now compute $m^*_{\mathrm{LP}}(\theta, \Omega)$.

In principle we could proceed along the lines suggested by the calculation above, i.e., compute $m^*(R, \theta, \Omega)$ and take

$$m^*_{\mathrm{LP}}(\theta, \Omega) = \lim_{R\to 1}[m^*(R, \theta, \Omega)]. \tag{10}$$

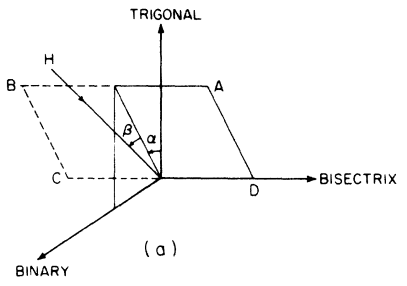

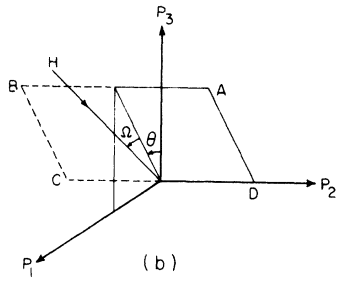

FIG. 3. Definition of magnetic field direction in (a) crystallographic-axis system and (b) ellipsoid principal-axis system. In both cases plane ABCD is rotated counter clockwise about the bisectrix or p_2 axis as one looks along it in the negative direction. β and Ω are angles in these rotated planes. The rotation about the bisectrix or p_2 axis is specified as occurring first.

A more straightforward method is to use the equation[16]

$$m^*_{LP} = [\,|\,v_F\,|\,(K)^{1/2}]^{-1}\,, \tag{11}$$

where v_F and K are the Fermi velocity and Gaussian curvature, respectively, at the limiting point. The calculation will be done in two steps: First, for a given field orientation, equations giving the location of the limiting point on the surface are calculated in terms of Cartesian coordinates, i.e., equations of the form $p_1' = p_1'(\theta, \Omega)$, $p_2' = p_2'(\theta, \Omega)$, and $p_3' = p_3'(\theta, \Omega)$, where (p_1', p_2', p_3') are the coordinates of the LP, are derived. Then, an equation of the form $m^*_{LP} = m^*_{LP}(p_1', p_2', p_3')$ is calculated using Eq. (11).

From the definition of the limiting point it is clear that it is located on the surface at that point where a plane normal to the magnetic field direction intercepts the Fermi surface at one point only. From symmetry it is clear that limiting points occur in pairs on each ellipsoid. To derive the coordinates of the limiting point, we compute the equations of a line whose direction is normal to the Fermi surface at the LP and which passes through the origin. From Eq. (3) and elementary solid geometry, the equations are easily found to be[17]

$$\frac{m_1 p_1}{p_1'} = \frac{m_2^2 E_g p_2}{m_2 \gamma E_g p_2' + r(p_2')^3} = \frac{m_3 p_3}{p_3'}\,. \tag{12}$$

The equations of a line parallel to the magnetic field direction which passes through the origin are given by

$$\frac{p_1}{\cos\Omega \sin\theta} = -\frac{p_2}{\sin\Omega} = \frac{p_3}{\cos\Omega\cos\theta}\,. \tag{13}$$

Equations (12) and (13) must represent the same line; hence, Eqs. (13), (12), and (3), and Eq. (3) evaluated at (p_1', p_2', p_3') represent six equations in the six unknowns p_1, p_2, p_3, p_1', p_2', and p_3'. These may be solved in a straightforward manner to yield the following series of equations:

$$2r^2(p_2')^6 + rm_2E_g(4\gamma+\rho)(p_2')^4 + 2m_2^2E_g^2\gamma(\gamma+\rho)(p_2')^2 - 4m_2^3E_g^2E(1+\lambda)\rho = 0, \tag{14}$$

$$(p_1')^2 = \frac{m_1^2\rho[2E(1+\lambda) - \gamma(p_2')^2/m_2 - r(p_2')^4/2m_2^2E_g]}{m_2\cot^2\theta\tan^2\Omega}\,, \tag{15}$$

$$(p_3')^2 = \frac{m_3}{m_1}\left(\frac{m_2}{m_1}\frac{\cot^2\theta\tan^2\Omega}{\rho} - 1\right)(p_1')^2, \tag{16}$$

where

$$\rho = \frac{m_2\tan^2\Omega}{(m_3 + m_1\tan^2\theta)}\,. \tag{17}$$

Equations (14)–(16) are the equations for the location of the limiting point in terms of Ω and θ. Having obtained the location of the limiting point, we now use Eq. (11) to compute the LP effective mass in terms of p_1', p_2', and p_3'.

The Fermi velocity magnitude at the limiting point is given by

$$|\,v_F\,| = |\,\nabla_{\vec{p}}\,E(\vec{p})\,|\Big|_{\vec{p}=(p_1', p_2', p_3')} \tag{18}$$

and is calculated to be

$$|\,v_F\,| = \frac{1}{\omega}\left[\left(\frac{p_1'}{m_1}\right)^2 + \left(\frac{\gamma p_2'}{m_2}\right)^2 + \left(\frac{p_3'}{m_3}\right)^2 + \frac{r(r+1)\gamma}{m_2^3E_g}(p_2')^4 + \frac{r^2(r+1)^2(p_2')^6}{4m_2^4E_g^2}\right]^{1/2}, \tag{19}$$

where $\omega = 1 + 2\lambda - (1-r)(p_2')^2(1/2m_2E_g)$. The Gaussian curvature is computed by first rewriting Eq. (3) in vector form as

$$\vec{p}_r = p_2\hat{p}_2 + p_1\hat{p}_1 + \left(\frac{m_3}{2}\right)^{1/2}\left[4E(1+\lambda) - \frac{2p_2^2\gamma}{m_2} - \frac{p_2^4 r}{m_2^2E_g} - \frac{2p_1^2}{m_1}\right]^{1/2}\hat{p}_3\,, \tag{20}$$

where $\vec{p}_r$ is a radius vector from the origin to the surface, and then using the following equation[18]:

$$K = \frac{A_1A_2 - B^2}{C_1C_2 - D^2}\,, \tag{21}$$

where

$$A_i = \frac{\partial\hat{n}}{\partial p_i}\cdot\frac{\partial\vec{p}_r}{\partial p_i}\,, \quad B = \frac{1}{2}\left(\frac{\partial\hat{n}}{\partial p_1}\cdot\frac{\partial\vec{p}_r}{\partial p_2} + \frac{\partial\hat{n}}{\partial p_2}\cdot\frac{\partial\vec{p}_r}{\partial p_1}\right),$$

$$C_i = \left(\frac{\partial\vec{p}_r}{\partial p_i}\right)^2, \quad D = \frac{\partial\vec{p}_r}{\partial p_1}\circ\frac{\partial\vec{p}_r}{\partial p_2}\,,$$

and $\hat{n}$ is the unit outward normal to the surface. The computation required is very lengthy, and we proceed directly to the answer. Evaluating the result of Eq. (21) at the limiting point and substituting it and Eq. (19) into Eq. (11) gives

$$m^*_{LP} = \frac{(2m_3E)^{1/2}(1+\lambda)\zeta}{\nu v_F}\left\{\frac{\left[\frac{m_2}{m_1}x^2 + \frac{\mu^2}{(1+\lambda)} + \frac{m_2}{m_3}z^2\right]\left[\nu^2 + \frac{m_3}{m_2}\mu^2(1+\lambda)\zeta\right]\left(\frac{m_1}{m_3}z^2 + x^2\right)}{\zeta^2[\mu^2 + \nu\gamma + 6\lambda\nu r y^2] - \mu^2z^2x^2\left[\frac{m_1}{m_3} - 1\right]^2}\right\}^{1/2}, \tag{22}$$

where

$$x^2 = (p_1')^2/[2m_1(1+\lambda)E], \quad y^2 = (p_2')^2/2m_2E, \quad z^2 = (p_3')^2/[2m_3(1+\lambda)E],$$

$$\zeta = (m_1/m_3)x^2 + z^2, \quad \mu = \gamma y + 2\lambda r y^3, \quad \nu = 1 + \lambda - \gamma y^2 - r\lambda y^4\,.$$

Obtaining the final expression for $m^*_{LP}(\alpha,\beta)$ requires one more set of equations: the transformation for each ellipsoid from its principal-axis system to the crystallographic-axis system. The equations are derived in I and we repeat them here for reference:

$$\sin\Omega = -\sin\phi\cos\theta_t\cos\beta\sin\alpha + \cos\phi\cos\theta_t\sin\beta + \sin\theta_t\cos\beta\cos\alpha, \tag{23}$$

$$\tan\theta = \frac{\cos\phi\sin\alpha + \sin\phi\tan\beta}{\sin\phi\sin\theta_t\sin\alpha - \cos\phi\sin\theta_t\tan\beta + \cos\theta_t\cos\alpha}, \tag{24}$$

where θ_t is the angle of tilt of the Fermi surface (equal to about $-6.3°$ for the data of EK), and $\phi = 0°$, $120°$, $-120°$ for the m^*_I, m^*_{II}, and m^*_{III} ellipsoids, respectively. In summary, to find $m^*_{LP}(\alpha,\beta)$, one computes Ω and θ from Eqs. (23) and (24), substitutes into Eqs. (14)–(16) to find p'_1, p'_2, and p'_3, and in turn substitutes these values into Eq. (22) to find the LP mass.

Although it is not immediately obvious, one can rewrite Eq. (22) in a form where E and E_g enter only as the ratio $\lambda = E/E_g$. Hence, there are only two adjustable parameters: λ and r. In general they are both independent and can assume any value. For Bi, however, we can appeal to experiment and find that there is a condition which the two parameters must meet. One can easily show[6] from Eq. (3) that the areas of the normal sections increase with p_2 near $p_2 = 0$, if

$$r > 1 \quad \text{and} \quad \lambda > 1/(r-1); \tag{25}$$

i.e., the Fermi surface is reentrant if Eq. (25) is satisfied. If the surface were reentrant, two large periods in $1/H$ would appear in quantum oscillation experiments for $\vec{H}$ near the p_y axis, rather than one, because of the two extremal areas. Since no such doubling of the periods has been observed in any de Haas–van Alphen or de Haas–Schubnikov experiment in Bi, we must require that

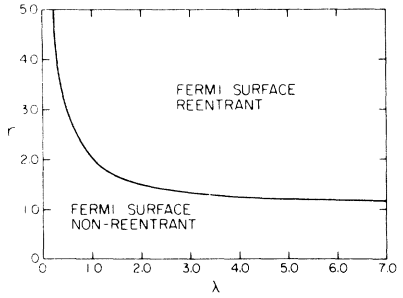

FIG. 4. Values of $r(=m_2/m'_2)$ and $\lambda(=E/E_g)$ which give a reentrant and nonreentrant Fermi surface, according to the NENP model [Eq. (2)]. The curve is the boundary between the two regions and is given by Eq. (26).

$$\lambda < 1/(r-1). \tag{26}$$

This inequality is plotted in Fig. 4.

III. COMPARISON WITH DATA OF EDEL'MAN AND KHAIKIN

EK performed their cyclotron-resonance experiments at a frequency of 9 GHz on samples of three different orientations: I, the normal to the sample $\vec{N}$ parallel to the binary axis; II, $\vec{N}$ parallel to the trigonal axis; and III, the binary axis perpendicular to $\vec{N}$, with the angle between the trigonal axis and $\vec{N}$ being 84°. Orientation III causes the plane of the sample to be the p_2 plane in the principal-axis system of one of the ellipsoids. The experimental values of the effective-mass tensor components at the Fermi level, deduced from the CO-mass data of EK in a manner described in the Appendix, are

$$m'_1 = 0.0059, \quad m'_2 = 1.304, \quad m'_3 = 0.011. \tag{27}$$

These are the values which are used in Eqs. (A5)–(A7) and whence in Eqs. (14)–(16) and Eqs. (22)–(24) to compute the LP-mass curves.

Figures 5(a) and 5(b) are graphs designed as

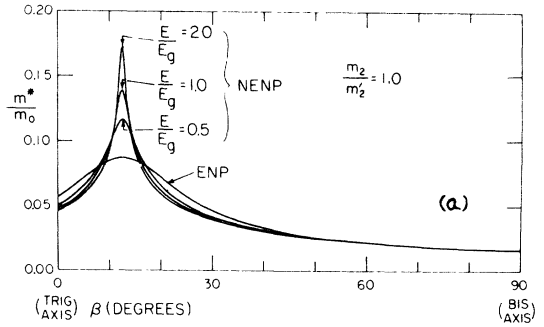

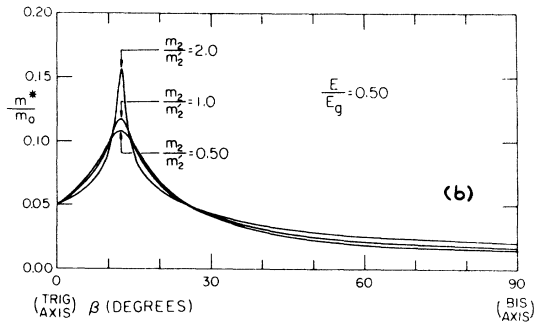

FIG. 5. NENP model theoretical angular variation of the limiting-point cyclotron effective mass m^*_{II}. The curves are computed from Eqs. (22)–(24), (27), and (A5)–(A7). β refers to Fig. 3(a) with $\alpha = 0$. (a) m_2/m'_2 is constant and E/E_g is a parameter. (b) E/E_g is constant and m_2/m'_2 is a parameter.

TABLE I. Electron LP masses of EK (Ref. 1) analyzed in this paper. See the beginning of Sec. III for an explation of the sample orientations.

Case No.	*EK*[a] designation	Sample orientation	Conventional designation	Fig. No.
1	$\beta_{2,3}$	I	m_{II}, m_{III}	6
2	β_1	I	m_I	7
3	β_2	III	m_{II}	8
4	γ_1	II	m_I	9

[a]Reference 1.

examples to show the type of LP-mass anisotropies predicted by the NENP model. Figure 5 is typical in that significant differences between the ENP and NENP models and significant changes in the curves as a function of changes in the values of the two parameters occur only near the directions of $\vec{H}$ where the cyclotron effective mass is a maximum.

Most of the LP data displayed by EK is in fact confined to these angles. In Table I we list the four such cases given by EK and identify them by the more common notation; in Sec. IV we will analyze them in detail, but we make some general comments here. Cases 1–3 are all very similar in their characteristics and are shown in Figs. 6–8. The criteria for fitting the curves to the data in all cases involved matching the data point at the peak to the theoretical curve; originally, it was hoped that the best values for r and λ could then be chosen unambiguously on the basis of the best fit to the remaining points. Unfortunately, the

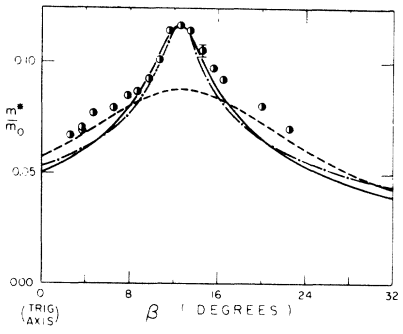

FIG. 6. Angular variation of the limiting-point cyclotron effective mass m_{II}^* ($=m_{III}^*$) for the magnetic field in the binary plane (referred to as case 1 in Table I). The experimental points are from Fig. 3 of Ref. 1. The solid curve ($\lambda=0.50$ and $r=1.0$) and dash-dot curve ($\lambda=0.18$ and $r=3.0$) are computed from the NENP model [Eq. (22)]; the dashed curve is the ENP model. β refers to Fig. 3(a) with $\alpha=0$.

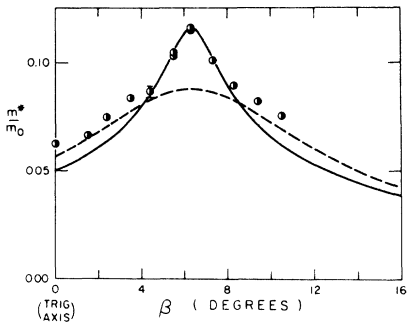

FIG. 7. Angular variation of the limiting-point cyclotron effective mass m_I^* for the magnetic field in the binary plane (referred to as case 2 in Table I). The experimental points are from Fig. 3 of Ref. 1. The solid curve is computed from the NENP model [Eq. (22)] with $\lambda=0.50$ and $r=1.0$; the dashed curve is the ENP model. β refers to Fig. 3(a) with $\alpha=0$.

general shape of the curve is relatively insensitive to the various combinations of r and λ, once the peak theoretical and experimental values have been matched. As an example, in Fig. 6 we have demonstrated this point by plotting curves for two widely different combinations of r and λ for case 1. As is evident, it is difficult to say that one curve fits the points any better than the other. The situation is the same for cases 2 and 3, although for simplicity we have chosen only to plot the curve for the parameter values $r=1.0$ and $\lambda=0.5$. Case 4 is shown in Fig. 9. Although the NENP curve com-

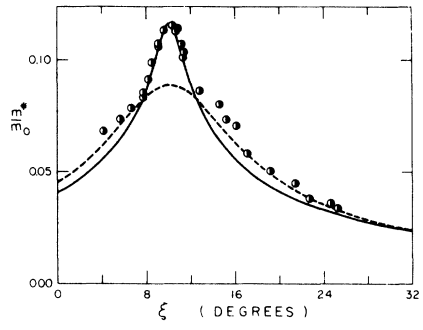

FIG. 8. Angular variation of the limiting-point cyclotron effective mass m_{II}^* for the magnetic field in a plane rotated about the binary axis approximately 6° from the trigonal axis (referred to as case 3 in Table I). The plane is approximately the p_2 plane in the principal-axis system of ellipsoid I. The experimental points are from Fig. 5A of Ref. 1. The solid curve is computed from the NENP model [Eq. (22)] with $\lambda=0.50$ and $r=1.0$; the dashed curve is the ENP model. ξ is an angle such that its complement is the angle between the magnetic field and the binary axis.

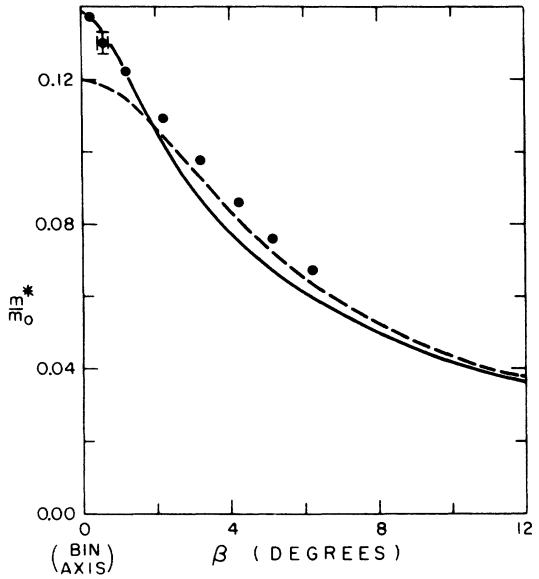

FIG. 9. Angular variation of the limiting-point cyclotron effective mass m_I^* for the magnetic field in the trigonal plane (referred to as case 4 in Table I). The experimental points are from Fig. 4 of Ref. 1. The solid curve is computed from the NENP model [Eq. (22)] with $\lambda = 0.23$ and $r = 1.0$; the dashed curve is the ENP model. β refers to Fig. 3(a) with $\alpha = 90°$.

pares with the experimental points in a manner similar to the other three cases, the various combinations of the two parameters needed to match theory and experiment at $\beta = 0°$ (the location of the effective-mass peak) are considerably different from the combinations required for cases 1–3. This difference is demonstrated by Fig. 10. Whereas the curves for cases 1–3 are essentially identical, the curve for case 4 departs radically from the others. The original motivation for plotting the curves in Fig. 10 was to determine if they intersected at any point; a point common to all four cases would presumably give the best determination of r and λ. However, since the curves do not intersect, an unambiguous determination of r and λ by comparing the LP-mass theory and experiment is not possible. We discuss some of the implications of the theory and of Figs. 6–10 in Sec. IV.

IV. DISCUSSION

Perhaps the most important conclusion to be drawn from Figs. 6–9 is that the NENP model is capable of explaining at least qualitatively the existence of a LP effective mass different from the CO effective mass in Bi. Within about 5°–10° of the peak the points fit the NENP model reasonably well, but beyond this interval the NENP model underestimates the experimental points by about 10%.

The best one can do to interpret the results quantitatively is to assume a value for one of the parameters (r or λ) and, from Fig. 10, determine a value for the other parameter. The difficulty with this procedure, of course, is that neither r nor λ has been determined with any high degree of confidence. A large number of experiments[7,11–14] have produced results consistent with assuming a value $r \simeq 1.0$; however, as mentioned in Sec. I, the de Haas–Shubnikov results of BEM[12] gave $r \simeq 3.0$. We shall initially assume that $r = 1.0$. From Fig. 10, this value for r gives a value $\lambda = 0.5$ for cases 1–3 and gives $\lambda = 0.23$ for case 4. The only direct measurement of λ (independent of any assumed model) was made by Esaki and Stiles[19] using tunneling spectroscopy, and they found $\lambda = 0.75$. Values derived from experiment using the ENP and NENP models have ranged from 0.5 [11] to 2.0 [12]; in general, the values derived on the basis of the NENP model tend towards the lower number. The basic problem in obtaining an accurate measurement of λ in pure Bi is the rather high sensitivity of the Fermi energy to any impurities present because of the low carrier concentration in pure Bi. The value $\lambda = 1.7$, derived from magneto-optical data,[7] has frequently been quoted as the generally accepted value of λ for pure Bi, although to the author's knowledge there is no reason for $\lambda = 1.7$ to be a better value than $\lambda = 0.75$, the directly measured value. In I we found that the de Haas–van Alphen data of Bhargava[11] in conjunction with the effective mass values of EK supported the NENP model with a value of $\lambda = 0.50$. In short the value $\lambda = 0.50$ required for cases 1–3 seems reasonable for pure Bi. A discrepancy does exist, however, for case

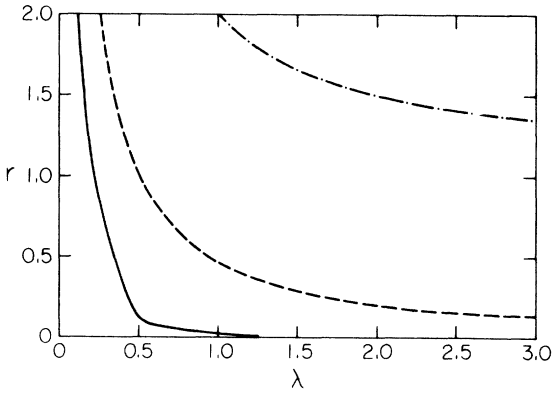

FIG. 10. Values of r and λ which match the LP cyclotron effective masses given by the NENP model with experiment at the peak in the anisotropy curves of Figs. 6–9. The dashed curve is for Figs. 6–8, all of which are essentially coincident; the solid curve is for Fig. 9. The dash-dot curve is the boundary between a reentrant and nonreentrant Fermi surface, taken from Fig. 5.

1 when it is compared with the corresponding CO-mass data (EK do not present CO-mass data for cases 2 and 3), since in I we found that a value of $\lambda = 1.7 \pm 0.5$ was required for a good fit to the NENP model for the CO-mass data of case 1. The need for widely different values of λ for the CO and LP masses is probably a result of the approximations used in deriving Eq. (2). A more positive conclusion would require more cases in which both CO- and LP-mass data points are known.

The low value of $\lambda = 0.23$ required for case 4 could be explained within the context of the NENP model in at least two ways. One, the sample used had an undetected acceptor impurity in it and thereby lowered the Fermi level below the pure Bi value. Or, two, if a data point had been taken for the field exactly parallel to the binary axis, it would have been somewhat higher than $m^*/m_0 = 0.138$, which is the value at $\beta = 0^0$ for $\lambda = 0.23$, and hence λ would be larger. The value 0.23 was selected, for lack of more information, by assuming that the value of m^*/m_0 at $\beta = 0°$ is approximately the same as the value at $\beta = 0.25°$, the nearest experimental point. The first possibility seems unlikely, since very-high-purity Bi is easily obtained. The second possibility probably explains at least part of the low value of λ, particularly since the curves of Fig. 4 show that near the effective mass maxima, the NENP model predicts a rather sharply peaked dependence. Experimental points from the other two electron masses (m_{II}^* and m_{III}^*) near the effective mass maxima would clarify the situation, but EK do not present this data. EK also give the CO-mass experimental points for case 4 and they were compared in I with the NENP model. We found that the fit to the NENP model was no better than the fit to the ENP model; the points agreed fairly closely with the ENP model, or in other words the points also compare well with the NENP model with a low value of λ, say between 0 and 0.25. Hence, there is consistency for case 4 between the LP-mass and CO-mass data within the context of the NENP model. This consistency actually gives some support to the hypothesis that an acceptor impurity was present in the sample of orientation II.

Since the value of $\lambda = 0.50$ found above is perhaps somewhat on the low side, it is logical to allow r to vary and determine what value of r brings λ more in line with other experiments. For cases 1–3 from Fig. 10 we find that $r = 0.65$ when $\lambda = 0.75$, and $r = 0.25$ when $\lambda = 1.7$. Hence, to increase λ, r must be made less than 1.0, whereas BEM found that $r \simeq 3$. If one were to assume that the Cohen model is accurate and valid in Bi in all respects, this result would seem to imply that the value of r found by BEM for Bi-Sn alloys does not apply to pure Bi. That is, this result indicates that the level of Sn doping needed to lower the Fermi level into the L-point valence band seriously distorts the band itself. On the other hand, if $r = 3$ is actually the pure Bi value, then a serious flaw in the NENP model is indicated. At the present time, we are unable to resolve completely this discrepancy. As stated before, many experiments have indicated that $r \simeq 1$; our results here strongly substantiate this value, and even suggest that $r < 1$. We hesitate, however, to attach too much quantitative significance to the values of r required to match the Cohen model and experiment, for the following reason. Several experiments[13,20,21] have indicated that bands other than the four used in Cohen's calculation leading to the NENP model are important in Bi. The four bands included in the NENP model are, in the notation of Golin,[6] L_5, L_6, L_7, and L_8. Normally, because of time reversal symmetry, L_5 and L_6 are degenerate, as are L_7 and L_8. In the two-band model[3] L_5 and L_6 form the conduction band and L_7 and L_8 form the valence band. The degeneracy is lifted in Cohen's calculation by the inclusion of spin-orbit coupling. We emphasize that these four bands are all fairly near the band gap. Interactions between these four bands and higher-order bands were initially included in the usual manner of $\vec{k} \cdot \vec{p}$ perturbation theory, but the higher band interactions were discarded by Cohen because the relevant band gaps were thought at the time of his work to be large enough (~ 1 eV) so that their effects could be neglected. Subsequent experimental work,[7,13] however, has shown that a band edge occurs much lower than 1 eV at $E \simeq 0.07$ eV, and this band clearly has some effect on the Fermi surface and cannot be neglected. Hence, the Cohen NENP model cannot be expected to be quantitatively accurate in all details.

In this regard we return to a point originally raised in I: Is it possible that the NENP model might explain the spin splittings observed[20] in pure Bi in large magnetic fields for the low-quantum-number Landau levels? As discussed in I, the energy-band calculation of Baraff[6] explains the spin splittings, but a rather large number of parameters are introduced in the process. The NENP model, it was hoped, might explain the spin splittings with no additional parameters required. It now appears that the NENP model is not successful in this regard. Basically, the NENP model is incapable of explaining a spin mass different from the orbital mass. This is not surprising, for, as Baraff[6] points out, Cohen's derivation of Eq. (2) neglects the antisymmetric part of the effective-mass tensor which gives rise to the spin energy. Hence, we probably should not expect the NENP model to explain high-field, low-quantum-number effects in which the spin is important. Rather, the NENP model seems well suited to low-field

phenomena such as cyclotron-resonance and quantum-oscillation experiments, such as the de Haas–van Alphen effect, for large quantum numbers.

V. CONCLUSIONS

The NENP model predicts a LP cyclotron effective mass which differs at some angles from the CO mass, unlike the ENP model. The fit of the data of EK to the NENP curves is clearly superior to the fit to the ENP model, although attempts to determine unambiguous values of m_2/m_2' and E/E_g from curve fitting were not successful. However, a value of $m_2/m_2' \simeq 1$ seems to fit the data best; this value is in general agreement with many experiments, but disagrees with the recent experiment of BEM, who find that $m_2/m_2' \simeq 3$. For $m_2/m_2' = 1.0$, we find in three of the four cases analyzed that the value $E/E_g = 0.50$ is required for a good fit and is a reasonable value for pure Bi. In the fourth case the anomalously low value $E/E_g = 0.23$ is required to fit the experimental points; the source of this discrepancy is not clear. In summary, combining the results of this paper and I, the Cohen NENP model, convenient because its dispersion relation is expressible in an analytic form, is capable of explaining some rather detailed structure observed in the cyclotron effective-mass anisotropy curves.

The results of this paper and of I are motivation for a careful, precise remeasurement of cyclotron resonance in pure Bi. The authors are presently undertaking this experiment in conjunction with surface-impedance quantum oscillations which we have observed to begin (at 24 GHz), at magnetic fields slightly above the highest cyclotron-resonance fundamental. Combining the effective-mass data of cyclotron resonance with the extremal-area data of the quantum oscillations allows us to analyze the data in terms of the NENP model in a manner suggested by Bhargava[9]: The ratio of the cyclotron effective mass to the cross-sectional area is a constant independent of magnetic-field direction for the ENP model; for the NENP model, however, the ratio is a fairly sensitive function of field orientation. This experiment should clarify some of the inconsistencies found above.

ACKNOWLEDGMENTS

It is a pleasure for the authors to thank Dr. G. E. Everett and Hans L. Churchill for many helpful conversations and for reading the manuscript.

APPENDIX

In this appendix we derive the equations relating the experimentally measured effective-mass tensor components to the bottom-of-the-band values used in the NENP model. Customarily, the three experimental values are referred to as m_1^*, m_2^*, and m_3^*, where the subscripts refer to the ellipsoid principal axis which is parallel to the magnetic field. The Fermi-level effective-mass tensor components (m_1', m_2', and m_3') are then computed on the basis of an ellipsoidal-parabolic model, i.e.,

$$m_1' = (m_2^* m_3^*)/m_1^*,$$
$$m_2' = (m_1^* m_3^*)/m_2^*, \tag{A1}$$
$$m_3' = (m_1^* m_2^*)/m_3^*.$$

The values given in Eq. (27) are obtained from Eq. (A1) by substituting for m_1^*, m_2^*, and m_3^* from the data of EK. We now require equations which relate the m_i^* to the NENP bottom-of-the-band values of the effective-mass tensor components, m_i. For the case $r = 1$ these equations can be obtained directly from Eq. (7) in I. For $r \neq 1$ the derivation of the necessary equations proceeds exactly as the CO effective-mass calculation in I, except that the computation of the derivative $\partial a/\partial E$ (a is the extremal area) is more complicated when $r \neq 1$. The results are

$$m_1^* = (2/\pi r)(m_2 m_3)^{1/2}(1 + \lambda + \lambda r)^{1/2}[K(k) + (r-1)\epsilon(k)], \tag{A2}$$

$$m_2^* = (m_1 m_3)^{1/2}(1 + 2\lambda), \tag{A3}$$

$$m_3^* = (2/\pi r)(m_1 m_2)^{1/2}(1 + \lambda + \lambda r)^{1/2}[K(k) + (r-1)\epsilon(k)], \tag{A4}$$

where

$$k^2 = r\lambda/(1 + \lambda + \lambda r)$$

and $K(k)$ and $\epsilon(k)$ are complete elliptic integrals of the first and second kinds, respectively. Substituting from Eq. (A1) into Eqs. (A2)–(A4) and solving for the m_i gives

$$m_1 = m_1'/(1 + 2\lambda), \tag{A5}$$

$$m_2 = \left(\frac{\pi}{2}\right)^2 \frac{r^2(1 + 2\lambda)\, m_2'}{(1 + \lambda + \lambda r)[K(k) + (r-1)\epsilon(k)]^2}, \tag{A6}$$

$$m_3 = m_3'/(1 + 2\lambda). \tag{A7}$$

Equations (A5)–(A7) are the desired equations.

*Work supported by National Science Foundation Grant.

[1]V. S. Edel'man and M. S. Khaikin, Zh. Eksperim. i Teor. Fiz. 49, 107 (1965) [Soviet Phys. JETP 22, 77 (1966)].

[2]D. Shoenberg, in *Progress in Low-Temperature Physics*, edited by C. J. Gorter (Interscience, New York, 1957), Vol. 2, Chap. 8.

[3]B. Lax, Rev. Mod. Phys. 30, 122 (1958); Bull. Am. Phys. Soc. 5, 167 (1960).

[4]When considering only the anisotropy of the cyclotron

effective masses, as we do in this paper, the ENP and EP models are identical, i.e., they result in the same curve when plotting m^* vs magnetic field orientation. In this paper we will refer to the two models collectively as the ENP model.

[5]R. J. Dinger and A. W. Lawson, Phys. Rev. 1, 2418 (1970).

[6]M. H. Cohen, Phys. Rev. 121, 387 (1961). Strictly speaking, the models for Bi which result from the calculations of S. Golin [*ibid.* 166, 643 (1968)] and G. A. Baraff [*ibid.* 137, A842 (1965)] are also nonellipsoidal and nonparabolic, but as in I we shall use NENP to refer solely to the Cohen model.

[7]R. N. Brown, J. G. Mavroides, and B. Lax, Phys. Rev. 129, 2055 (1963).

[8]Y. H. Kao, Phys. Rev. 129, 1122 (1963).

[9]R. N. Bhargava, Phys. Rev. 156, 785 (1967).

[10]R. T. Bate, N. G. Einspruch, and P. J. May, Phys. Rev. 186, 599 (1969).

[11]D. Weiner, Phys. Rev. 125, 1226 (1962).

[12]L. C. Hebel and P. Wolff, Phys. Rev. Letters 11, 368 (1963).

[13]G. A. Antcliffe and R. T. Bate, Phys. Letters 23, 622 (1966).

[14]W. E. Engeler, Phys. Rev. 129, 1509 (1963).

[15]In the NENP model the pieces which make up the Fermi surface are distorted from a true ellipsoid and are frequently referred to as quasiellipsoids. For convenience we will use the term ellipsoid even when discussing the NENP model.

[16]M. Ia. Azbel' and E. A. Kaner, J. Phys. Chem. Solids 6, 113 (1958).

[17]T. S. Peterson, *Elements of Calculus* (Harper and Row, New York, 1960), p. 372.

[18]T. J. Willmore, *Introduction to Differential Geometry* (Clarendon Press, Oxford, England, 1959).

[19]L. Esaki and P. J. Stiles, Phys. Rev. Letters 14, 902 (1965).

[20]G. E. Smith, G. A. Baraff, and J. M. Rowell, Phys. Rev. 135, A1118 (1964).

[21]G. A. Antcliffe and R. T. Bate, Phys. Rev. 160, 531 (1967).

PHYSICAL REVIEW B VOLUME 3, NUMBER 2 15 JANUARY 1971

Resonant Energy Transfer between Localized Electronic States in a Crystal*

T. F. Soules
Lighting Research Laboratory, General Electric Company
Nela Park, Cleveland, Ohio 44112

and

C. B. Duke
Department of Physics, Materials Research Laboratory, and Coordinated Science Laboratory,
University of Illinois, Urbana, Illinois 61801 *and Lighting Research Laboratory,*
General Electric Company, Nela Park, Cleveland, Ohio 44112

(Received 13 April 1970)

We propose a model Hamiltonian to describe resonant energy transfer between discrete electronic states each of which is coupled to the same boson field. In this model, the calculation of the transition probabilities for resonant energy transfer, radiationless intraimpurity electronic transitions, and phonon-broadened electromagnetic transitions among the electronic states of a given impurity are rendered formally equivalent, differing only in the selection of various model parameters. The relation of those parameters to microscopic models is described in detail for the case of resonant energy transfer between localized impurity states. A calculation of the energy-transfer probability is presented which is valid to arbitrary order in the electron-phonon interaction, but is the linear-response-theory treatment of the electronic-transfer term. Explicit comparison between the predictions of our model and those of the Förster-Dexter model are given. We present an analysis of the time-dependent Schrödinger equation which permits us to distinguish between dissipative and multiply periodic solutions to the Schrödinger equation and gives a *precise* definition of weak- and strong-coupling limits. Finally, we indicate the application of our results to describe experimental systems involving radiationless energy transfer and electronic relaxation in rare-earth impurities in crystals.

I. INTRODUCTION

Recently there has been considerable interest in energy transfer between localized states in a wide variety of connections – including sensitized luminescence, exciton diffusion, molecular electronic relaxation, polaron conduction, and energy transfer in biological systems, to name a few. We discuss the transfer of energy between two impurity ion states which, in addition to being coupled to each other, are coupled to the same quasicontinuous modes of vibration of a crystal lattice.[1] We propose this simplified semiphenomonological Hamiltonian in order to describe the absorption (emission) of